Scalelength of disc galaxies

Fathi, Kambiz; Allen, Mark; Boch, Thomas; Hatziminaoglou, Evanthia; Peletier, Reynier F.

Published in:
Monthly Notices of the Royal Astronomical Society

DOI:
10.1111/j.1365-2966.2010.16812.x

Publication date:
2010

Monthly Notices
of the
ROYAL ASTRONOMICAL SOCIETY

Mon. Not. R. Astron. Soc. **406,** 1595–1608 (2010) doi:10.1111/j.1365-2966.2010.16812.x

Scalelength of disc galaxies

Kambiz Fathi,[1,2]★ Mark Allen,[3] Thomas Boch,[3] Evanthia Hatziminaoglou[4] and Reynier F. Peletier[5]

[1]*Stockholm Observatory, Department of Astronomy, Stockholm University, AlbaNova Center, 106 91 Stockholm, Sweden*
[2]*Oskar Klein Centre for Cosmoparticle Physics, Stockholm University, 106 91 Stockholm, Sweden*
[3]*Observatoire de Strasbourg, UMR 7550, Strasbourg 67000, France*
[4]*European Southern Observatory, Karl-Schwarzschild-Str. 2, 85748 Garching bei München, Germany*
[5]*Kapteyn Astronomical Institute, Postbus 800, 9700 AV Groningen, the Netherlands*

Accepted 2010 April 7. Received 2010 April 2; in original form 2010 February 18

ABSTRACT

We have derived disc scalelengths for 30 374 non-interacting disc galaxies in all five Sloan Digital Sky Survey (SDSS) bands. Virtual Observatory methods and tools were used to define, retrieve and analyse the images for this unprecedentedly large sample classified as disc/spiral galaxies in the LEDA catalogue. Cross-correlation of the SDSS sample with the LEDA catalogue allowed us to investigate the variation of the scalelengths for different types of disc/spiral galaxies. We further investigate asymmetry, concentration and central velocity dispersion as indicators of morphological type, and are able to assess how the scalelength varies with respect to galaxy type. We note, however, that the concentration and asymmetry parameters have to be used with caution when investigating type dependence of structural parameters in galaxies. Here, we present the scalelength derivation method and numerous tests that we have carried out to investigate the reliability of our results. The average *r*-band disc scalelength is 3.79 kpc, with an rms dispersion of 2.05 kpc, and this is a typical value irrespective of passband and galaxy morphology, concentration and asymmetry. The derived scalelengths presented here are representative for a typical galaxy mass of $10^{10.8\pm0.54}$ $M_{\odot}$, and the rms dispersion is larger for more massive galaxies. Separating the derived scalelengths for different galaxy masses, the *r*-band scalelength is 1.52 ± 0.65 kpc for galaxies with total stellar mass 10^{9}–10^{10} $M_{\odot}$ and 5.73 ± 1.94 kpc for galaxies with total stellar mass between 10^{11} and 10^{12} $M_{\odot}$. Distributions and typical trends of scalelengths have also been derived in all the other SDSS bands with linear relations that indicate the relation that connect scalelengths in one passband to another. Such transformations could be used to test the results of forthcoming cosmological simulations of galaxy formation and evolution of the Hubble sequence.

Key words: galaxies: structure.

1 INTRODUCTION

The exponential scalelength of a galaxy disc is one of the most fundamental parameters to determine its morphological structure as well as to model its dynamics, and the fact that the light distributions are exponential makes it possible to constrain the formation mechanisms (Freeman 1970). The scalelength determines how the stars are distributed throughout a disc, and can be used to derive its mass distribution, assuming a specific M/L ratio. Ultimately, this mass distribution is the primary constraint for determining the formation scenario (e.g. Lin & Pringle 1987; Dutton 2009, and referenced therein), which dictates the galaxy's evolution. As the galaxy evolves, substructures such as bulges, pseudo-bulges, bars, rings and spiral arms may build up, and this will then considerably change the morphology of the host discs (Combes & Elmegreen 1993; Elmegreen et al. 2005; Bournaud, Elmegreen & Elmegreen 2007). The scalelength value is intimately connected to the circular velocity of the galaxy halo, which in turn relates closely to the angular momentum of the halo in which the disc is formed (Dalcanton, Spergel & Summers 1997; Mo, Mao & White 1998). Up to the last few years, cosmological simulations were limited to rather low resolution, were discs and spheroids were barely resolved, and generally limited to high redshifts, so reproducing realistic disc scalelengths for modern galaxies was clearly out of reach. The current simulations reach resolutions that allow resolving the discs from high redshift down to redshift zero, and subtle mechanisms changing the disc masses and scalelengths can be studied

★E-mail: kambiz@astro.su.se

(e.g. Ceverino, Dekel & Bournaud 2010; Governato et al. 2010; Martig & Bournaud 2010; Schaye et al. 2010), thus calling for a comprehensive observational determination of these parameters to test the state of the art cosmological simulations.

Previous observations of NGC, UGC and low surface brightness galaxies have shown that scalelengths span over a range of three orders of magnitudes (e.g. Boroson 1981; Romanishin, Strom & Strom 1983; van der Kruit 1987; Schombert et al. 1992; Knezek 1993; de Jong 1996). Any physical galaxy formation scenario should be able to explain this wide range of values while simultaneously explaining the similarities among disc galaxies throughout this range.

Analytic disc formation scenarios predict that, in cases where angular momentum is conserved, the disc scalelength is determined by the angular momentum profile of the initial cloud (Lin & Pringle 1987), and the scalelength in a viscous disc is set by the interplay between star formation and dynamical friction (Silk 2001). These processes form the basis of a galaxy's gravitational potential, and determine the strength of gravitational perturbations, the location of resonances in the disc, the formation and evolution of spiral arms and bars, kinematically decoupled components in centres of galaxies, and the dynamical feeding of circumnuclear starbursts and nuclear activity (e.g. Elmegreen et al. 1996; Fathi 2004; Knapen 2004; Kormendy & Kennicutt 2004).

Photometrically, one generally derived this scalelength by azimuthally averaging profiles of the surface brightness which is in turn decomposed into a central bulge and an exponential disc, and when spatial resolution allows other components such as one or several bars and rings can be taken into account.

As images in different bands probe different optical depths and/or stellar populations, it is likely that a derived scalelength value should depend on waveband, and these effects may vary as a function of galaxy type where different amounts of dust and star formation are expected. Dusty discs are more opaque, resulting in larger scalelength values in bluer bands when compared with red and/or infrared images. Similar effects can also be caused by differences in the stellar populations. Differences in scalelength as a function of passband can therefore be used to derive information about the stellar structure and contents of galactic discs. Both the effects of stellar populations and dust extinction have been subject to much discussion over the years (e.g. Simien & de Vaucouleurs 1983; Kent 1985; Valentijn 1990; Peletier et al. 1994, 1995; van Driel et al. 1995; Beckman et al. 1996; Courteau 1996; Baggett, Baggett & Anderson 1998; Cunow 1998, 2001, 2004; Graham 2001; Graham & de Blok 2001; Prieto et al. 2001; Giovanelly & Haynes 2002; MacArthur, Courteau & Holtzman 2003; Graham & Worley 2008). A detailed and extensive analysis of the dust effects has also been presented for a few tens of galaxies in Holwerda (2005) and subsequent papers by this author, however, as noted by Peletier et al. (1994) and van Driel et al. (1995), the scalelength alone in different wavelengths in small sample cannot be used to break the age/metallicity and dust degeneracies. Investigating the scalelength variation as a function of inclination for large numbers of galaxies is necessary to distinguish between the effects of dust and stellar populations.

The common denominator in all the previous studies is the roughly comparable sample sizes (at most few hundred galaxies). Most studies have so far analysed individual galaxies, or samples containing a few tens, and in unique cases a few hundred (e.g. Knapen & van der Kruit 1991; Courteau 1996) galaxies. Although a number of great results from studies with the Sloan Digital Sky Survey (SDSS; York et al. 2000) in the last years have appeared, these works have not studied the astrophysical parameters targeted here.

As a part of a European Virtual Observatory[1] Astronomical Infrastructure for Data Access (Euro-VO AIDA) research initiative, we have undertaken a comprehensive analysis of the scalelength in disc galaxies using an unprecedentedly large sample of disc galaxies. We have used the Virtual Observatory (VO) tools to retrieve data in all (u, g, r, i and z) bands from the sixth SDSS major data release (DR6; Adelman-McCarthy et al. 2008) which includes imaging catalogues, spectra and redshifts freely available. We use the LEDA[2] catalogue (Paturel et al. 2003) to retrieve morphological classification information about our sample galaxies, and those with types defined as Sa or later are hereafter refereed to as disc galaxies (distribution of both samples is presented in Fig. 1).

In the present paper, we present the data retrieval and analysis method used to automatically derive the scalelengths for a sample of disc galaxies which contains 56 096 objects (described in Section 2), and after rigorous tests described in Section 3, we find that a subset of 30 374 of these can be called reliable following these criteria. The scalelengths presented here relate only to the disc components, and we have tried to avoid the regions that could be dominated by the bulge component, in order to avoid complications related to the uncertainties of bulge–disc decomposition procedure (as demonstrated in e.g. Knapen & van der Kruit 1991). In Section 4 we present the first results based on our unprecedentedly large sample of galaxies and finally discuss their implications in Section 5.

2 SAMPLE GALAXIES FROM SDSS

2.1 First selection criteria

The DR6 provides imaging catalogues, spectra and redshifts for the third and final data release of SDSS-II, an extension of the original SDSS consisting of three subprojects: the Legacy Survey, the Sloan Extension for Galactic Understanding and Exploration and a Supernova Survey. The SDSS Catalogue Archive Server Jobs System[3] allow for a sample selection based on a number of useful morphological and spectroscopic parameters provided for all objects. We use these parameters and make a first selection of the entire SDSS DR6 sample. Various VO methods were investigated to perform the download of the SDSS images, and the SkyView[4] was chosen for this task. This service has the advantage of being able to create fits cut outs centred at a given sky coordinate and with a given size. Moreover, SkyView is able to rescale the image backgrounds to the same level, hence correcting for background level differences between the SDSS tiles.

The image size is an important parameter to achieve a reliable sky subtraction which is necessary to derive realistic scalelengths, thus we require that the images cover an area at least three times the size of each galaxy. To optimize the data handling and keep low data transfer time from SkyView, we chose a constant image size of 900×900 pixels to be sampled for all galaxies, still being able to achieve a reliable sky subtraction. With these specifications, the image size is 3.2 MB with the typical download time of 16 s per

[1] http://www.euro-vo.org
[2] http://leda.univ-lyon1.fr
[3] http://casjobs.sdss.org
[4] http://skyview.gsfc.nasa.gov

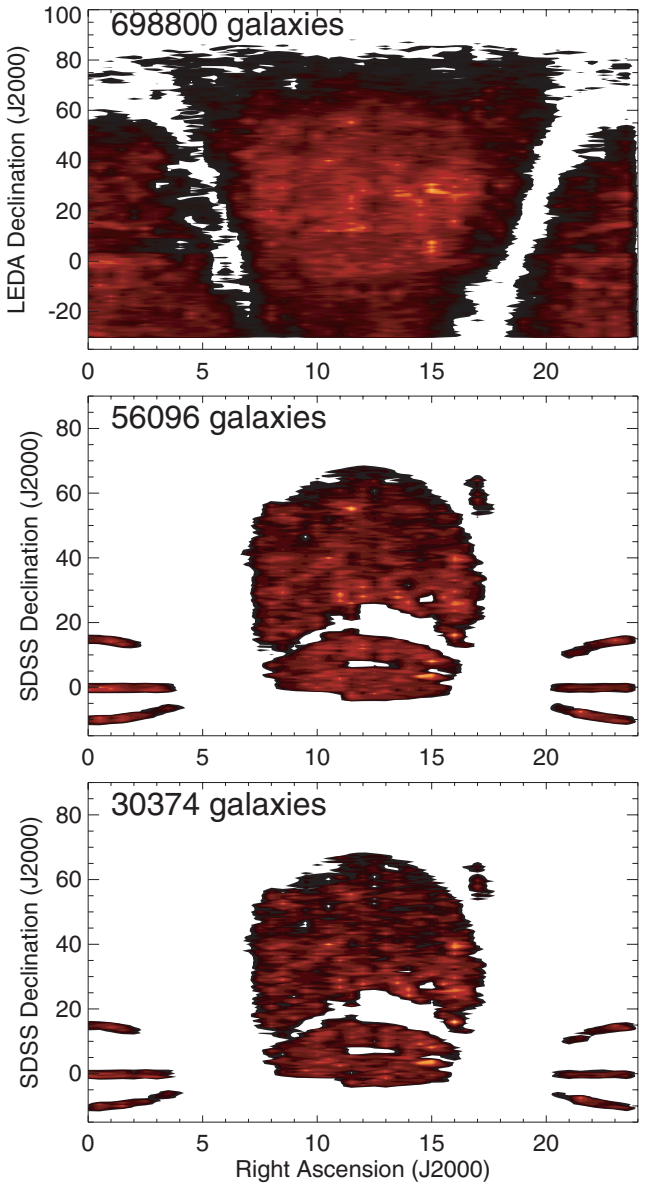

Figure 1. Top: right ascension and declination distribution of the galaxies for which the LEDA services provide a Hubble classification number $\geq$1 (irrespective of classification error). Middle: same for the 56 096 SDSS galaxies fulfilling the first sorting criteria described in Section 2.1. Bottom: the final sample of 30 374 selected SDSS disc galaxies for which we have reliable scale *r*-band scalelengths (regardless of uncertainty in the morphological classification, see also Section 3.3).

image. This also includes the time that SkyView spends cutting, mosaicing and rescaling images.

Our first selection criteria use SDSS parameters to ensure the following.

(1) The object is a galaxy, and has good quality images available, i.e. quality keyword $\geq$2.

(2) The galaxy is at a position with low *r*-band Galactic extinction $A_r \leq 1.0$. In reality, we find that 99 per cent of the sample have $A_r \leq 0.25$.

(3) For each galaxy SDSS provides spectroscopic redshift measurement, i.e. galaxy *r*-band magnitude $\leq$17.7.

(4) The galaxy diameter is at least 60 pixels (=24 arcsec) and at most 200 pixels (=80 arcsec in diameter). The first criterion ensures that the derived light profile samples the disc with at least 10 data points (for 2-pixel wide rings) to derive the scalelength, and the second criterion is for an optimized data retrieval procedure described above. Here we use the *r*-band isophotal semimajor axis *isoA* and semiminor axis *isoB* as a measure for the galaxy size.

(5) High inclination (incl. $\geq$70°) galaxies are removed to avoid selection effect problems, but also since scalelengths for such systems are not reliable. The inclination is determined using the ratio between the semiminor axis *isoB* and semimajor axis *isoA* in the *r* band from the SDSS parameter list ($\cos i = isoB/isoA$).

(6) No redshift cut was applied, however, Fig. 2 shows that the sample extends out to redshift 0.3, with the typical redshift at $\log z = -1.2$ derived with $\geq$0.995 confidence level, and with 15 per cent of the sample with $\log z \geq -1.0$.

This first set of criteria leaves us with a total of 95 735 galaxies. We use the LEDA services to retrieve a numeric Hubble classification parameter *T* for the galaxies in our sample (more on this in Section 4.1). We first download the entire LEDA catalogue, which we cross-correlate with the SDSS sample using TOPCAT[5] and only select the galaxies which, in LEDA, are classified as spiral galaxies (i.e. $1 \leq T \leq 8$). A total of 56 096 Sa–Sd (i.e. *T* between 1 and 8) spiral galaxies (see Fig. 1) were found, for which SDSS *u*, *g*, *r*, *i*, *z*-band images were downloaded. In Section 4.1, we further discuss whether all these galaxies are well-classified disc or spiral galaxies.

In Fig. 2, we show the distribution of some key parameters retrieved from the SDSS and LEDA data base. This figure shows that the different sample selection stages do not introduce any biases in our sample. It should be noted that, at this stage, we are unable to determine whether the galaxies in our sample are isolated or disturbed systems, as this information is not provided by any of the catalogues we have used. We make this distinction using the asymmetry parameter described in Schade et al. (1995).

2.2 Scalelengths from SDSS

The first issue that arises at this point is the fact that SDSS services provide users with the disc scalelength as well as de Vaucouleurs effective radius for each galaxy (in all bands), and that, in principle, these values could be used to carry out our analysis. In Fig. 3, we show that the values provided by the SDSS services show anomalies that are beyond our satisfaction for carrying out our analysis. The plot shows peculiar systematic effects in their derivation of the de Vaucouleurs radii and scalelengths around some discrete values marked by the overdensities, the source and explanations for which we cannot find. We thus decide to recalculate the scalelengths.

3 DERIVING SCALELENGTHS AND ASYMMETRIES

3.1 Using IDL and GDL

To derive the disc scalelength, we use some important parameters provided by the SDSS in order to constrain galaxy geometry as well as the location of the sky region. These are semiminor axis *isoB*, semimajor axis *isoA*, isophotal position angle *isoPhi*, and for consistency, we use these *r*-band quantities also in all other bands.

[5]http://www.starlink.ac.uk/topcat

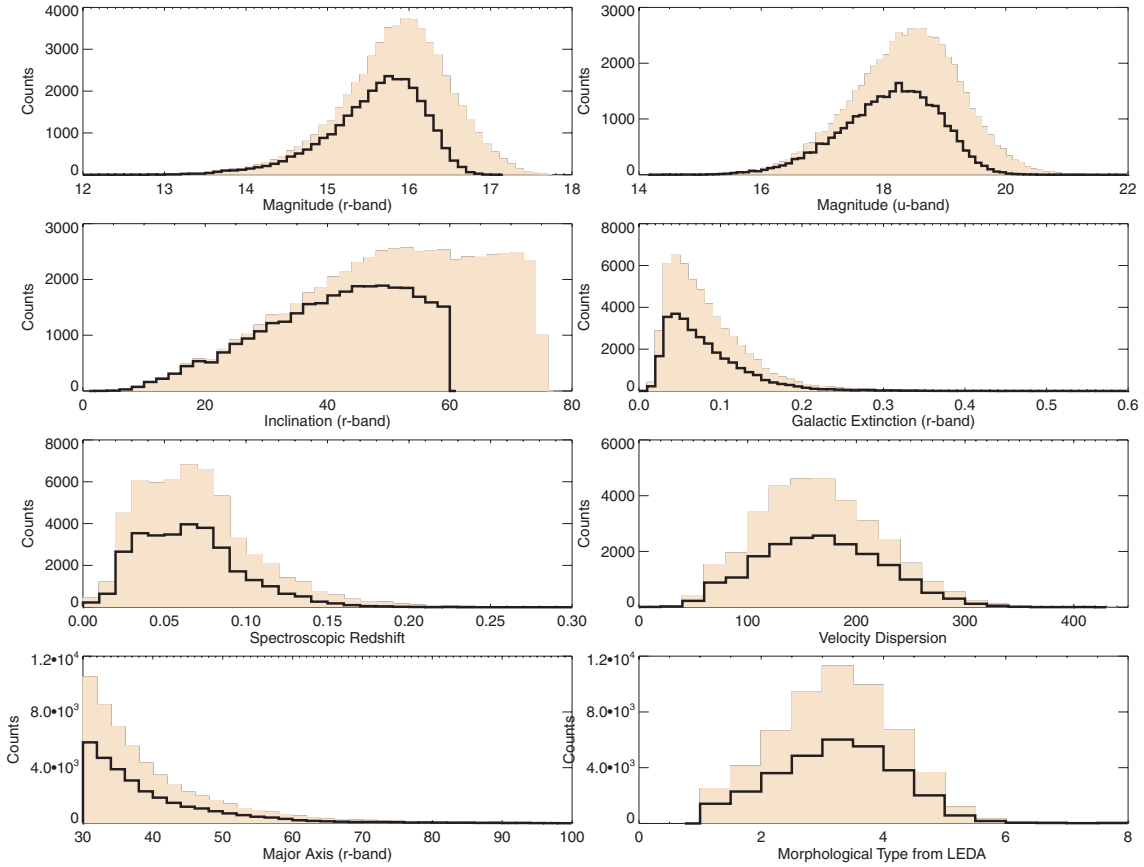

Figure 2. Distribution of some key parameters retrieved from the SDSS data base and morphological types from LEDA (bottom right). The filled histograms are the 56 096 disc galaxies described in Section 2.1, and the open histograms show the distributions of the final 30 374 galaxies for which we derive reliable scalelengths. The distribution of the sample remains unchanged.

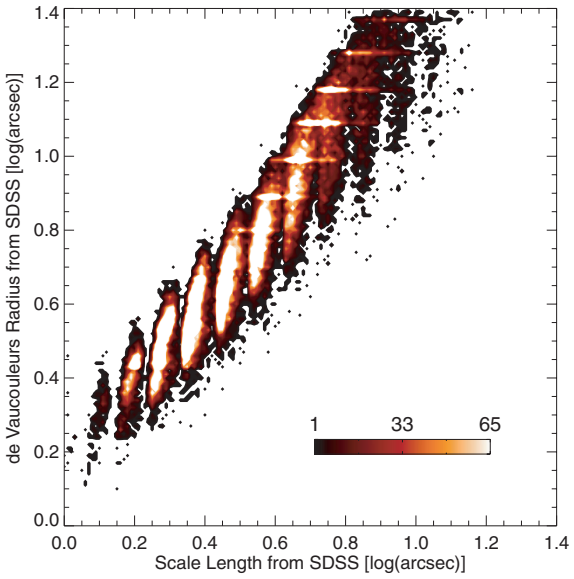

Figure 3. Density plot of the de Vaucouleurs effective radius (y-axis) versus exponential disc radius (x-axis) provided by the SDSS service for the entire disc galaxy sample. The odd clustering of the data (overdensities around discrete values) show the strong systematic effects in these two parameters provided by the SDSS team.

Our scalelength derivation routine uses standard IDL routines, though due to license limitations this code can only be executed once, and hence is estimated to take a long time to run. Using one single IDL session, we would need 47 d to derive the scalelengths for the entire sample, thus in order to speed up the process, we decided to run this computation on a cluster of machines located at Centre de Données astronomiques de Strasbourg CDS. Since the freely available IDL virtual machine does not allow one to launch batch queries, and since installing an IDL licence on each cluster node was not an option, we used the open source clone of IDL, GNU Data Language (GDL; Coulais et al. 2009). We found out that a few IDL functions were either missing or behaving improperly, thus requiring minor tweaking in our code. Then, we ran both IDL and GDL code on the same subset of SDSS images, in order to check the reliability of the GDL output.

Once the GDL code was installed on each node of the cluster, the 56 096 SDSS images were put to an iRods[6] installation deployed at CDS. Finally, the scalelength computation was launched on the cluster, using the following architecture.

(i) A JAVA program holds the list of galaxies to process, and – for each object of this list – sends a message to the cluster, asking to spawn a new job (i.e. launch the corresponding computation).

[6]iRods (www.irods.org) is a distributed data management system, which provides a distributed storage environment to easily store and share files.

(ii) The cluster master node receives the request, and dispatches it to the cluster node with the smallest CPU load.

(iii) The cluster node then downloads from iRods the *u*, *g*, *r*, *i*, *z* images corresponding to the galaxy to process, runs the GDL code and sends back the computed result to iRods.

(iv) If the computation fails, it will be resent to another node until success.

The CDS cluster has proven to be very stable and reliable, though some problems were found in the dispatching algorithm, resulting sometimes in overloading some of the nodes while some others were idle. Four nodes of the cluster were dedicated to our computation. As the total computation time is roughly proportional to the number of involved nodes, allocating 10 times more nodes would have decreased this time by a factor of 10. This would only be true if the computation service were to be close to the data, so that the transfer time would be negligible with respect to the computation time. In theory, on the CDS cluster, with four dedicated nodes, we should have been able to process 11 200 galaxies d^{-1}, however, in reality, the cluster only processed between 8500 and 9000 galaxies d^{-1}, which could be explained by some inefficiency in the dispatching algorithm. To conclude, using the CDS, we have been able to derive the scalelengths for all 56 090 galaxies in all five SDSS bands in less than a week.

3.2 The procedure

The procedure to derive scalelength and calculate asymmetry parameters from the SDSS images is illustrated in Fig. 4 and carries out the following steps.

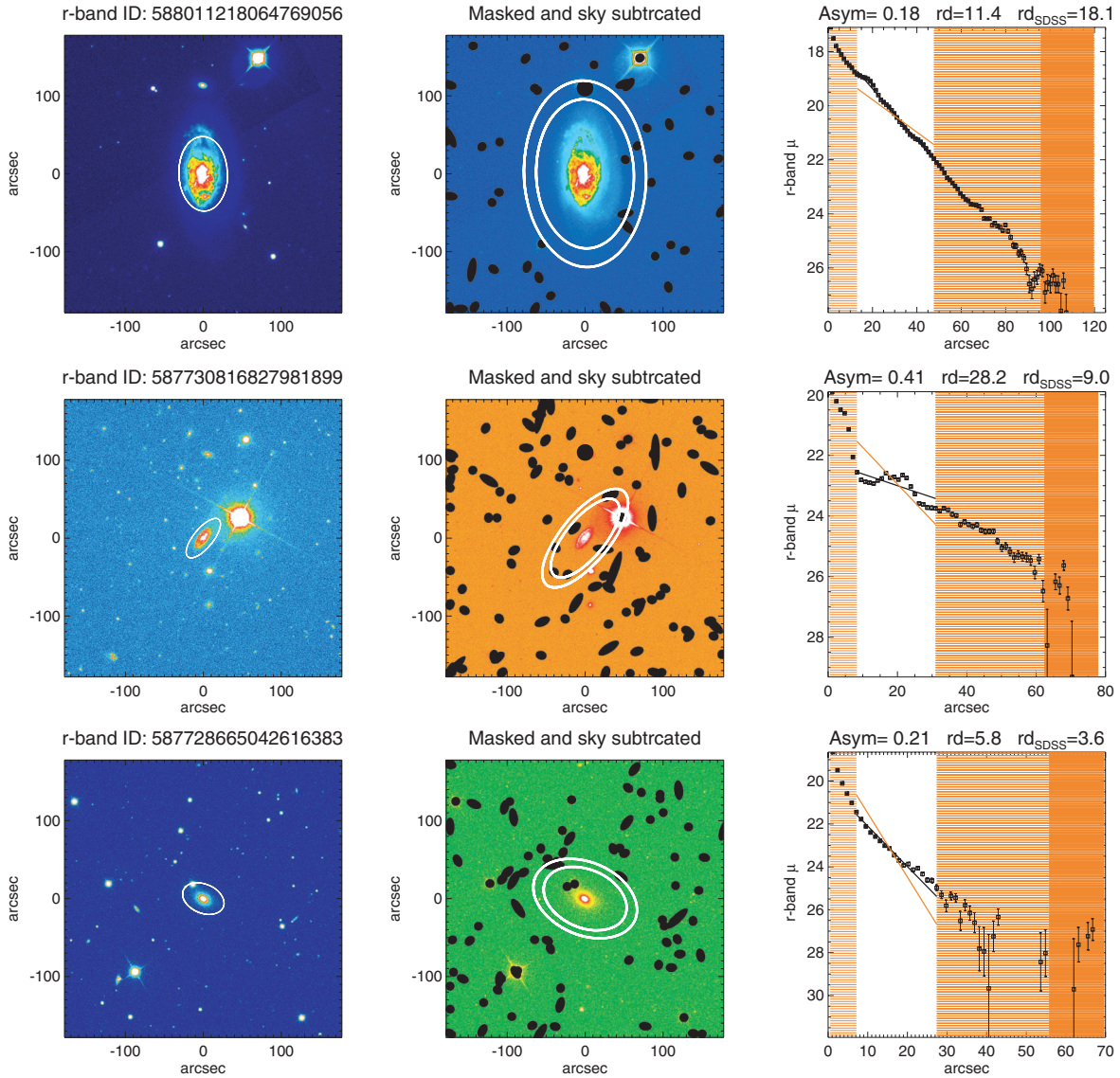

Figure 4. Three randomly selected galaxies for which we illustrate the procedure for deriving the scalelength (see Section 3). For each galaxy, the left-hand panel shows the *r*-band image and the ellipse with axis-ratio *isoB*/*isoA*. The middle panel shows the sky-subtracted image, the sky region $2.0 \pm 0.25 \times$ *isoA* outlined by two corresponding ellipses and the SExtractor sources masked. The right-hand panel shows the light profile using the zero-point from the SDSS, and linear fit to the disc region as described in Section 3. At the top of this panel, the asymmetry parameter, our derived disc scalelength (black linear fit) and the scalelength from SDSS (arbitrarily shifted red line) are stated.

(i) Reading the image and assigning the pre-determined *r*-band parameters from a file that contains all SDSS parameters for the entire sample.

(ii) Selecting the sky region as the ellipse encompassing the range $2.0 \pm 0.25 \times isoA$. This is marked as a darker shaded region in the rightmost panels in Fig. 4. The mean value of this region, using Tukey's bi-weight mean formalism described in Mosteller & Tukey (1977), is used to calculate the sky level for sky subtraction as well as setting the background level.

(iii) To remove foreground stars and point sources from the image, we extract point sources with SExtractor (Bertin & Arnouts 1996), by selecting all point sources that are larger than 4 pixels in size and more than 3σ above the background level. All pixels belonging to these sources are then masked out, and we note that our selection could include bright star-forming regions and small background galaxies in these sources.

(iv) Using the asymmetry parameter definition of Schade et al. (1995) and Conselice (2003), we calculate the asymmetry parameter:

$$A = \sum \|I - I_{180}\| \Big/ \sum I, \tag{1}$$

where I is the sky subtracted galaxy image intensity and I_{180} is that for the image rotated by 180° around the galaxy centre. It should be noted here that the asymmetry criterion applied here removes ongoing mergers and galaxies with companions at a projected distance of about twice the galaxy radius, and here we take the results of Conselice (2003) at face value, that $A \geq 0.35$ means that the system is disturbed.

(v) Using the *isoB*, *isoA*, *isoPhi* parameters from SDSS, we then section each galaxy into 2-pixel wide ellipses oriented at the major axis position angle *isoPhi* and with minor-to-major axis ratio $b/a = isoB/isoA$. The bi-weighted mean surface brightness value within each ellipse is calculated to compile the galactocentric surface brightness profile $\mu(r)$ for each galaxy.

In spatially resolved systems, surface brightness profiles are commonly fitted by a multiple of parametric functions in order to describe the contribution of different components to the observed profile. A de Vaucouleurs ($r^{1/4}$; de Vaucouleurs 1948) or Sérsic ($r^{1/n}$; Sérsic 1968) law is typically used for the innermost part of the disc, and for the outer parts an exponential function of the form

$$\mu(r) = \mu_0 + 1.086 \frac{r}{r_\mathrm{d}} \tag{2}$$

is used, where μ_0 is the central surface brightness, r is the galactocentric radius and r_d is the disc scalelength of the outer disc. In addition to these two components, other functions may be used to fit the halo component, bars, rings and other structures in the galaxies (e.g. Prieto et al. 2001), and the fits can be applied to one-dimensional light profiles or directly on two-dimensional images (Byun & Freeman 1995). Here we fit equation (2) to the one-dimensional surface brightness profiles.

Running the fully automated fitting algorithm on all retrieved images, we found a number of artefacts which cause problems for applying the code successfully. These include the following.

(i) SkyView does not deliver the image for the galaxy in all bands, i.e. a blank image has been transferred and stored. The first query delivered 892 blank images, and a second query on the blank images delivered successfully less than 1 per cent of the images.

(ii) The galaxy is positioned such that there are no adjacent tiles observed yet, and thus a large part of the retrieved image is filled by SkyView with blank pixels.

(iii) The galaxy is too faint in a given band to deliver reliable surface brightness profile, i.e. the linear fit results in a negative slope.

(iv) Man-made satellites passing too close to the galaxy position.

3.3 Reliable scalelengths

Saturated stars near the objects cannot be masked properly using SExtractor (due to undetermined source radii). Moreover, strong galaxy interactions and noisy images introduce errors in the derived scalelengths. We select randomly a few hundred images for which we plot the surface brightness profiles with corresponding linear fits. Visual inspection showed that the routine runs as expected. Saturated stars, if far away from a galaxy (farther than $2.25 \times isoA$, i.e. the outermost sky pixel) do not introduce any errors in the derived parameters as they are not considered at any stage. If close to a galaxy, they can be regarded as interactions. Interactions between galaxies can be quantified following. Conselice (2003) and Conselice et al. (2003) who found that interacting or merging galaxies mostly have asymmetry parameter $A \geq 0.35$.

When applying equation (1), it is crucial to rotate the images around the centre of the galaxy, as minor offsets can significantly overestimate A. We apply a centroid fitting to our sample, and find that the images generated by SkyView are off-centred by about half a pixel. This offset, although minor in terms of pixels and arcseconds, significantly overestimates A for our galaxies (see Fig. 5).

If the galaxy image is deep enough, it is expected that the scalelength values in two adjacent bands should be similar. As images in all SDSS bands are not equally deep, we investigate the *r*- and *i*-band images for this purpose only, since these two filters are comparable, and sufficiently adjacent to deliver almost identical scalelengths. Plotting the corresponding scalelengths, shown in Fig. 6, we find that galaxies with high inclination (incl. $\geq 60°$) are the objects that introduce the large scatter in this diagram.

We use Pearson's product moment correlation coefficient to calculate the coefficient of determination $\Re^2$ according to the standard

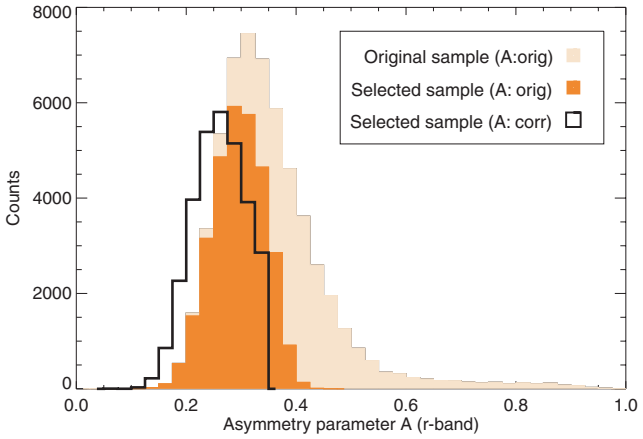

Figure 5. Asymmetry parameter for all 56 096 disc galaxies assuming the objects are located in the centre of the image (grey histogram), and when the galaxy image is rotated around the 'true' galaxy centre found by centroid fitting (red histogram). The final set of 30 374 low-inclination and low-asymmetry galaxies for which we derive the scalelengths are shown with the black histogram.

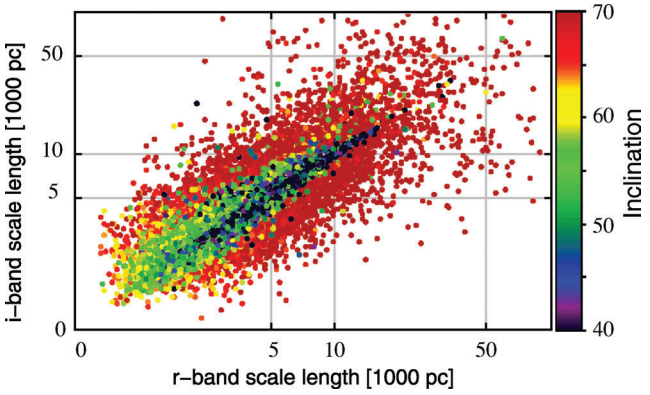

Figure 6. Scalelengths form the *i*-band images (*y*-axis) versus those from *r*-band images (*x*-axis), where the inclination of the galaxy is shown by the colour bar on the right of the figure. Although the points fall on a 1:1 slope, the galaxies with incl. $<60^\circ$ have smaller scatter ($\Re^2 > 0.90$, see text in Section 3.3).

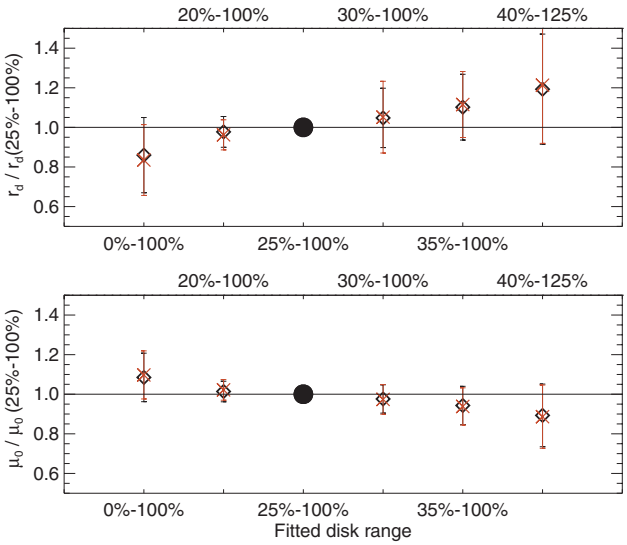

Figure 7. Disc scalelength and central surface brightness for different assumed disc range as a fraction of *isoA* parameter provided by the SDSS. The values illustrated here have been derived for a random subsample of 800 galaxies in *r* band (black diamonds) and *i* band (red crosses). All values have been normalized to that illustrated by the black circle, which is the disc range we assume throughout this work.

formula

$$\Re^2 = 1 - \frac{\sum_{j=1}^{N}(X_j - \hat{X}_j)^2}{\sum_{j=1}^{N}(X_j - \overline{X})^2},$$

where N is the number of data points, X_j are the measured data, $\hat{X}_j$ are the estimated values given by linear regression and $\overline{X}$ is the mean value of the measured data points. In simple statistical terms, the numerator is termed the total sum of squares, the denominator is the error sum of squares, the coefficient $\Re^2$ provides the per cent of the variation that can be explained by the linear regression equation, and therefore is a useful measure for the variance of one variable that is predictable from the other variable. If the regression line passes exactly through 50 per cent of the data points, it would be able to explain half of the variation of the linear fit, and would result in $\Re^2 = 0.5$. Throughout our analysis, we trust a correlation if $\Re^2 \geq 0.9$, and $\Re^2 \leq 0.68$ is considered insignificant (c.f., less than 1σ confidence level is insignificant).

The dispersion of the data points around the 1:1 line can is then measured by calculating $\Re^2$ for different inclination bins, and we find that this parameter remains above 0.90 for incl. ≤ 60, hence keep all the galaxies with incl. $\leq 60^\circ$. We will later find that combining the inclination and asymmetry restriction will deliver even higher coefficient of determination between the scalelengths in different bands.

Finally, we find that for five galaxies, the SDSS spectroscopic redshifts are larger than 1, whereas the rest of the sample has redshift <0.3. Despite the small redshift errors, we find the redshifts for these five galaxies unrealistic and we choose to remove them from our sample.

Thus, applying these cuts, we derive scalelengths for 30 374 disc galaxies that we argue are reliable, given the arguments mentioned above.

3.4 Disc and sky ranges

Here, we will not delve into the intricacies of fitting the light curves, but focus on the determination of the scalelength of the exponential disc. Despite the long tradition (see references in Section 1), the important and comprehensive study by Knapen & van der Kruit (1991) showed that the errors in these data are still significantly large ($\approx$25 per cent), especially if they were obtained from photographic plates. The uncertainties depend on image depth, image sky coverage, data reduction, disc region fitting, the order in which bulges, bars or other components are fitted. These matters become more complicated when analysing with SDSS images which are relatively shallow, and even more so when automatically fitting thousands of galaxies which cover a wide range of brightness and morphologies. To avoid complications that are not related to the nature of our analysis (e.g. Fathi & Peletier 2003), we have decided to derive the disc scalelength simply by fitting an exponential profile to a pre-defined disc region of each galaxy, i.e. the region where we assume the light to be dominated by the exponential profile. This means that we are simply cutting out the central regions of the galaxies where bulges and strong bars are expected.

We determine the disc region by empirically fitting the equation (2) to a set of ranges where we expect the disc to dominate the derived surface brightness profiles. We use the *isoA* parameter to estimate this range, and randomly select 800 galaxies, to which we apply this test both in *r* and *i* bands. In Fig. 7, we show the resulting disc scalelengths when fitting the regions presented in Table 1, and when normalized to our nominal 25–100 per cent of the *isoA* radius, we find that the derived scalelengths change by less than 10 per cent for a wide range of assumed disc ranges (seen as the unshaded region in the rightmost panels in Fig. 4). We further note that the distribution of the data points for each test, normalized to the 25–100 per cent *isoA* range, is well represented by a Gaussian, and the error bars in Fig. 7 are indeed symmetric.

For a similar test, we assume sky regions at different distances from each galaxy centre and assess the effect of the sky subtraction on the derived scalelengths. Applied to the same randomly selected 800 galaxies, we found that, assuming that the sky is represented by the $2.0 \pm 0.25 \times$ *isoA* region, robust scalelength and surface brightness measurements are delivered (see Fig. 8 and Table 2).

Table 1. Disc scalelength and central surface brightness for different assumed disc range as a fraction of *isoA* as illustrated in Fig. 7. The values presented here have been derived for a random subsample of 800 galaxies with formal errors given in brackets, and all values are normalized to the scalelength derived in the range 25–100 per cent.

Fitted *isoA* range	(r band) $\frac{r_d}{r_d(25-100\ \text{per cent})}$	(r band) $\frac{\mu_0}{\mu_0(25-100\ \text{per cent})}$	(i band) $\frac{r_d}{r_d(25-100\ \text{per cent})}$	(i band) $\frac{\mu_0}{\mu_0(25-100\ \text{per cent})}$
0–100 per cent	0.91(0.19)	0.87(0.18)	1.07(0.12)	1.09(0.12)
20–100 per cent	0.98(0.08)	0.97(0.07)	1.02(0.05)	1.03(0.05)
25–100 per cent	1	1	1	1
30–100 per cent	1.07(0.15)	1.09(0.18)	0.97(0.07)	0.96(0.08)
30–100 per cent	1.14(0.27)	1.12(0.17)	0.93(0.12)	0.93(0.09)
40–120 per cent	1.20(0.28)	1.25(0.29)	0.87(0.16)	0.87(0.16)

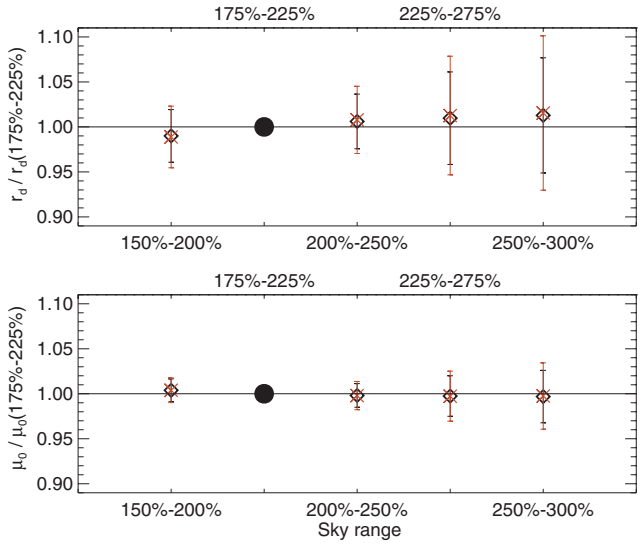

Figure 8. Disc scalelength and central surface brightness for different assumed sky range as a fraction of *isoA* parameter provided by the SDSS. The values illustrated here have been derived for a random subsample of 800 galaxies in r band (black diamonds) and i band (red crosses). The values have been normalized to that illustrated by the black circle, which is the sky range we assume throughout this work.

3.5 Scalelengths in *u, g, r, i, z* bands

Although the SDSS is one of the most influential and ambitious astronomical surveys, the depth of its images in all bands are not equal. Here we have chosen to analyse only the galaxies for which SDSS provides spectroscopic redshifts (in order to investigate the redshift evolution the parameters we derived), where SDSS is complete for r-band magnitude <17.7. The images in other bands are not equally deep and/or complete to this magnitude limit, partly due to the significantly different transmission curves for the different filters. Including atmospheric extinction and detector efficiency, the peak quantum efficiency of the system in u and z bands are $\approx$10 per cent, g and i bands $\approx$35 per cent and r band $\approx$50 per cent. Thus it is necessary to apply a magnitude cut which varies depending on the band, fainter than which we are not able to derive reliable scalelengths.

For each pair of SDSS filters, we expect that the scalelength variation larger than a factor of 1.5 is unphysical. We determine the magnitude limit for a pair of filters by plotting the scalelength ratio versus magnitude in one of the bands (see Fig. 9), and scan the values from the brighter to the fainter levels in fixed bins of 0.2 mag. Once we reach a magnitude where less than 95 per cent of the scalelength ratios is smaller than 0.67 or larger than 1.5 (i.e. above or below the horizontal dotted lines in Fig. 9), we stop the scan and select this value for the faintest magnitude level in that band for which we trust the scalelengths. As shown in Fig. 9, this procedure very clearly demonstrates the noise in different bands, and how the values presented in Table 3 have been established. In the given examples, the scalelengths in r band when compared to i band are complete to an r-band magnitude of 17.70 (indicated by the arrow), and the u versus z band is complete to a u-band magnitude of 16.29 (indicated by the arrow).

4 RESULTS

4.1 Scalelength versus morphology

The morphological classification scheme of Sandage (1961) is designed based on visual inspection of basic features of galaxies which relates them to their formation and evolution histories. While this classification scheme is somewhat subjective, in the past years, numerous efforts have been made to define quantitative versions of this classification scheme (e.g. Burda & Feitzinger 1992; Doi, Fukugita & Okamura 1993; Abraham et al. 1996; Yamauchi et al. 2005).

The numeric morphological types presented in the LEDA catalogue are a compilation of the morphological types encoded in the de Vaucouleurs scale as well as the luminosity class (van den Bergh's definition). There is also information about the presence of bars and rings, but we do not consider these for the present paper mostly

Table 2. Disc scalelength and central surface brightness for different assumed sky range as a fraction of *isoA* as illustrated in Fig. 8. The values presented here have been derived for a random subsample of 800 galaxies, normalized to the sky range 2.00 ± 0.25, with formal errors given in brackets.

Fitted sky range	(r band) $\frac{r_d}{r_d(2.0\pm0.25)}$	(r band) $\frac{\mu_0}{\mu_0(2.0\pm0.25)}$	(i band) $\frac{r_d}{r_d(2.0\pm0.25)}$	($i$band) $\frac{\mu_0}{\mu_0(2.0\pm0.25)}$
1.75 ± 0.25	0.99(0.03)	0.99(0.03)	1.00(0.01)	1.00(0.01)
2.00 ± 0.25	1	1	1	1
2.25 ± 0.25	1.00(0.03)	1.01(0.04)	1.00(0.01)	1.00(0.02)
2.50 ± 0.25	1.01(0.05)	1.01(0.07)	1.00(0.02)	1.00(0.03)
2.75 ± 0.25	1.01(0.06)	1.01(0.09)	1.00(0.03)	1.00(0.04)

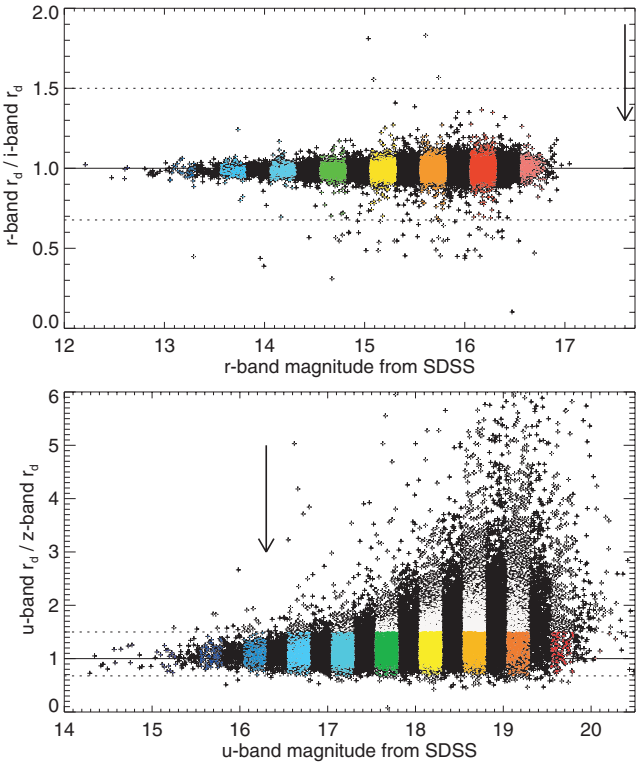

Figure 9. Scalelength ratio versus magnitude for two pairs from Table 3. Bins of 0.2 mag are used to scan the data points 'from left to right', and when less than 95 per cent of the ratios are inside the dotted lines, that magnitude limit is taken to be the faintest magnitude where we trust the scalelengths for these two bands. Here we show the best case *r*, *i* pair (top) and the worst case *u*, *z* pair (bottom). In each panel, the arrow indicates the cutting limit presented in Table 3.

Table 3. Magnitude cuts applied to the final sample of 30 374 galaxies as described in Section 3. To apply the cut to each pair, a plot similar to Fig. 9 was set up, and the magnitude cut was decided accordingly.

Filter pair	Upper magnitudes	Number of galaxies
g and *r*	$g < 17.70$ and $r < 17.70$	30 201
g and *i*	$g < 19.95$ and $i < 16.65$	30 371
g and *z*	$g < 17.70$ and $z < 15.53$	27 319
r and *i*	$r < 17.70$ and $i < 16.65$	30 374
r and *z*	$r < 17.70$ and $z < 15.53$	27 329
i and *z*	$i < 15.89$ and $z < 15.53$	27 264
u and *g*	$u < 16.79$ and $g < 14.94$	847
u and *r*	$u < 16.54$ and $r < 13.56$	132
u and *i*	$u < 16.79$ and $i < 13.14$	123
u and *z*	$u < 16.29$ and $z < 12.78$	88

since this information is only available for minor fraction of the sample. More details about the classification of galaxies can be found in the Level 5 of the NASA/IPAC Extragalactic Database (NED). The morphological types of LEDA have been compiled using from Vorontsov-Velyaminov, Arkipova & Kranogorskaja (1963–1974), Nilson (1973), Lauberts (1982), de Vaucouleurs et al. (1991) and Loveday (1996).

We select only the galaxies which are classified using the numeric type = 1 (i.e. Sa) up to and including numeric type = 8 (i.e. Sdm). Most of the values presented in Fig. 2 are subject to errors larger than 1, typically smaller for fainter galaxies, but they seem not

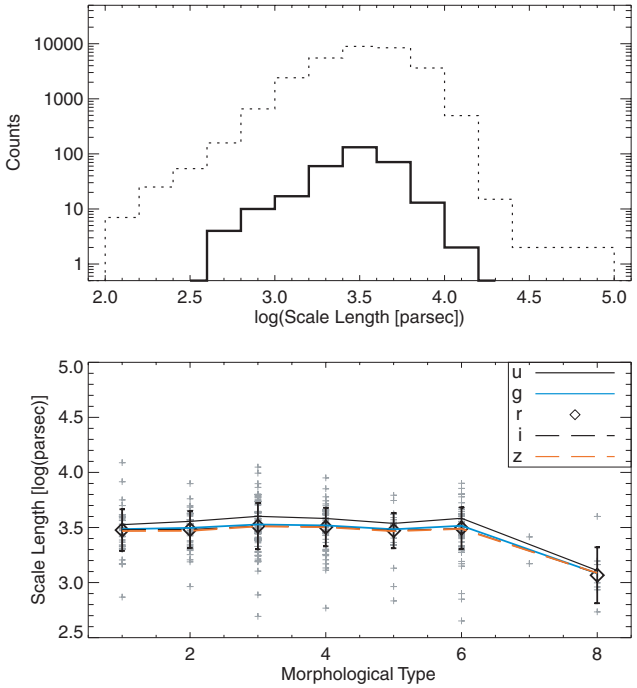

Figure 10. Top: distribution of the reliably derived *r*-band scalelengths for the entire sample of 30 374 galaxies (dotted histogram) and the 309 morphologically well classified galaxies (solid histogram). Bottom: scalelength versus morphological type for the 309 galaxies which have been morphologically classified accurately. The *r* band has been used with the scalelength in *u*, *g*, *i*, *z* bands, *i* plotted in the middle panel. The error bars for all bands are comparable, and here we only show these for the *r*-band values.

to depend much on other parameters such as asymmetry, redshift, etc. To analyse the dependency of the parameters with respect to morphological type, we strictly only use the galaxies for which the morphological type error is smaller than 0.5. These are 309 galaxies from our final sample of 30 374 galaxies, for which we investigate how the scalelength and asymmetry parameter depends on morphology.

Typically, scalelengths for disc galaxies are not expected to depend on Hubble morphological type (de Jong 1996; Graham & de Blok 2001) for types ranging between 1 and 6. Here, we analyse our derived values in this context first by only using the galaxies for which we only find morphological classifications with corresponding errors smaller than 0.5, i.e. the 309 galaxies explained in Section 4.1. In Fig. 10, we plot the *r*-band scalelength and morphological types, and find that our sample is fully consistent with previous results showing that the absolute value of the scalelength is independent of type. We transform the scalelength to parsec units by using the spectroscopic redshifts provided by the SDSS and ignore local flows. Our scalelength values agree with those derived by previous authors (e.g. van der Kruit 1987; de Jong 1996; Cunow 2001); we find that the average *r*-band scalelength for the entire sample is 3.79 ± 2.05 kpc, and that for the 309 galaxies with reliable morphology is 3.3 ± 1.6 kpc (see top panel of Fig. 10). Further discussion is provided in Section 4.2, and the errors are root mean square (rms) values.

In combination with the mass determination described in Section 4.3, we find that the mass does play a certain role in the behaviour of Fig. 10. Although out to type $T = 6$ scalelength are constant, the later type galaxies ($T > 6$) are generally those of lower mass, and hence in agreement with Fig. 11. However,

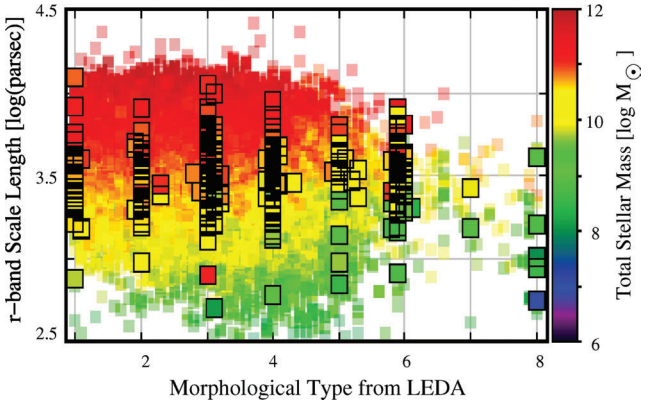

Figure 11. Scalelength versus morphological type for the entire sample of 30 374 galaxies, with the 309 well-classified galaxies marked with black squares. The colour represents the total stellar mass for each galaxy.

it should be noted that here we only have used the galaxies with robust morphological classification, and have a smaller number of low-mass galaxies as compared with high-mass galaxies (nine galaxies with total stellar mass 10^8–10^9 $M_\odot$, 40 galaxies with total stellar mass 10^9–10^{10} $M_\odot$ and 207 galaxies with total stellar mass 10^{10}–10^{11} $M_\odot$).a

We now cross-correlate our sample with the morphologically classified bright galaxy catalogue of Fukugita et al. (2007). Their catalogue contains 2275 galaxies classified by visual inspection of SDSS images in the *g* band. We find 283 objects overlapping between the two samples. The small overlap is partly due to the fact that around half of the objects in Fukugita et al. (2007) are early-type galaxies (RC3 type $T < 1$), and partly since it is essentially the overlap between the LEDA sample and that of Fukugita et al. (2007). Moreover, our sample has an upper limit for the galaxy sizes due to our preferred strategy for using SkyView (see Section 2.1). From this sample of 283 galaxies, only 45 galaxies have been accurately classified (their T error $\leq$1) in Fukugita et al. (2007). For these objects, we find weak correlation between the morphological classification from LEDA and those from Fukugita et al. (2007). In a similar fashion to Shimasaku et al. (2001), we define the *inverse* concentration parameter as the ratio between the radii containing 50 and 90 per cent of the Petrosian flux, respectively, r_{50}/r_{90} provided by the SDSS services. As a consistency check, we ensure that we reproduce fig. 10 of Shimasaku et al. (2001), i.e. that morphological classification provided by LEDA correlates with concentration parameter. Furthermore, we find that although the vast majority of our sample have very large morphological classification uncertainties (T error $\geq$1), the concentration parameters that we calculate for all 30 374 galaxies indicate that, in agreement with Shimasaku et al. (2001), they are disc galaxies.

Regarding the correlation of the concentration parameter with morphological type, for the 309 well-classified galaxies $\Re^2 = 0.31$, and for the full sample $\Re^2 = 0.16$. Although we find these values unconvincing as firm correlations, we acknowledge a clear trend that concentration parameter is increasing with galaxy morphological type. Likewise, the spread of points in asymmetry-type and velocity dispersion-type diagrams are very large, and the coefficients of determination even lower than that of the concentration parameter, however, here also the trend is acknowledged.

Given that robust morphological classification is known only for a very small subset of our entire sample, we invoke other parameters in order to be able to further investigate the scalelengths for the full

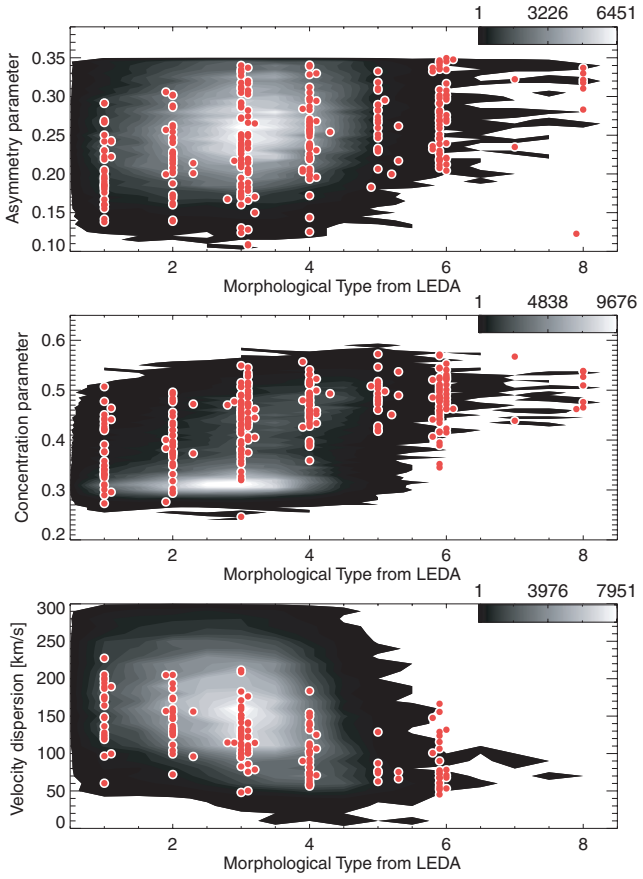

Figure 12. Asymmetry, concentration and velocity dispersion as type indicator for the full sample (grey density plot) and for accurately (type error $\leq$0.5) classified galaxies in LEDA.

sample. Following the above arguments, and their consistency with the previous findings by, e.g. Conselice (1997), Shimasaku et al. (2001) and Fukugita et al. (2007), we find it instructive to invoke these parameters as type indicators (see Fig. 12). For example, we find that the asymmetry parameter correlates with type T as $A = 0.19 + 0.02T$, put this into the graph, however, the $\Re^2$ varies between 0.05 and 0.81 depending on bin and choice of subsample and parameter, with the best correlation for unjustified binning applied. For this reason, we do not quote the errors or mathematical formulation for how A, C or velocity dispersion, vary with type, but take these trends as an indications and further investigate how scalelength depends on these parameters as morphological-type indicators.

In Fig. 13, we plot the scalelengths versus asymmetry, concentration and velocity dispersion. Although it is shown that scalelength decreases at higher concentration parameter, a line-fitting exercise reveals $\Re^2 = 0.12$, which implies insignificant correlation. The velocity dispersion has a higher correlation, $\Re^2 = 0.37$, but still with no strong statistical significance. Moreover, the large scatter of the scalelength values illustrated in Fig. 13 is consistent with the galaxies studied by de Jong (1996).

This exercise tells us, first, that asymmetry, concentration and velocity dispersion only correlate weakly with morphological type, and secondly, that even when using these parameters as morphological-type indicators, there is no strong change in disc scalelength for different galaxy types. Furthermore, we have now

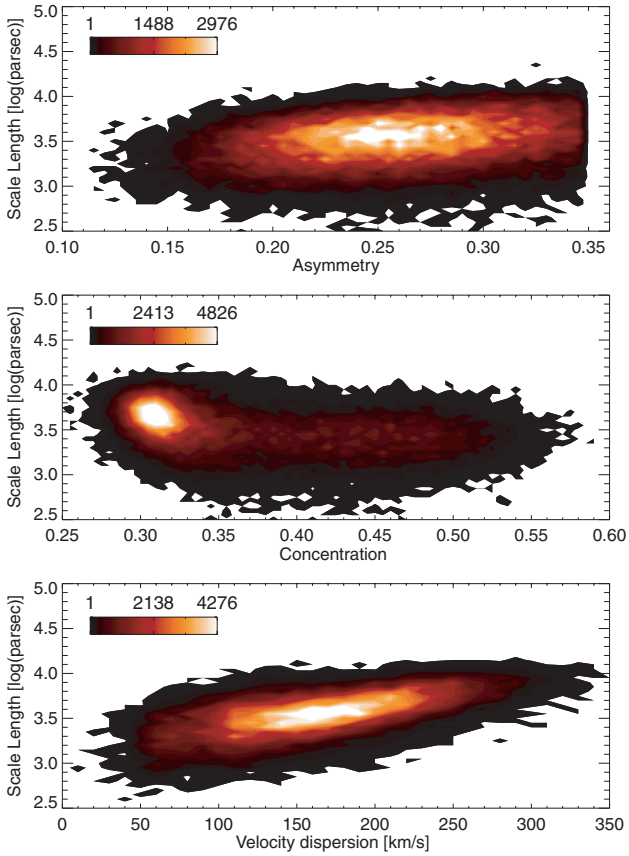

Figure 13. Scalelength versus asymmetry and concentration parameter and stellar velocity dispersion for the full sample of 30 374 galaxies.

been able to use the full sample of 30 374 galaxies with reliable scalelengths.

4.2 *u, g, r, i, z* scalelengths

The derived scalelengths can be compared between the images in different bands to investigate the effects of dust and stellar populations in disc galaxies (e.g. Cunow 2001). Such analysis is complementary to the results on colour gradients used to analyse age gradients in discs (e.g. Cunow 2004, and many more).

We analyse the derived scalelengths in different bands applying the limits presented in Table 3. We can then compare for a given subset, where reliable scalelengths have been derived in two bands, how the scalelength changes between different SDSS bands. We derive a series of correlations between the scalelengths in different bands, and although not all band-pair samples are of equal size, we find that the correlations for all the pairs are significant (see equations 3–12, where all formal errors and coefficients of determination are given, and Fig. 14):

$$\log\left(r_{\rm d}^{g}\right) = 0.25(\pm0.03) + 0.91(\pm0.01)\log\left(r_{\rm d}^{u}\right) \quad \Re^2 = 0.94, \quad (3)$$

$$\log\left(r_{\rm d}^{r}\right) = 0.36(\pm0.08) + 0.88(\pm0.02)\log\left(r_{\rm d}^{u}\right) \quad \Re^2 = 0.92, \quad (4)$$

$$\log\left(r_{\rm d}^{i}\right) = 0.32(\pm0.07) + 0.89(\pm0.02)\log\left(r_{\rm d}^{u}\right) \quad \Re^2 = 0.94, \quad (5)$$

$$\log\left(r_{\rm d}^{z}\right) = 0.36(\pm0.09) + 0.88(\pm0.03)\log\left(r_{\rm d}^{u}\right) \quad \Re^2 = 0.92, \quad (6)$$

$$\log\left(r_{\rm d}^{r}\right) = 0.06(\pm0.01) + 0.98(\pm0.01)\log\left(r_{\rm d}^{g}\right) \quad \Re^2 = 0.98, \quad (7)$$

$$\log\left(r_{\rm d}^{i}\right) = 0.10(\pm0.01) + 0.97(\pm0.01)\log\left(r_{\rm d}^{g}\right) \quad \Re^2 = 0.98, \quad (8)$$

$$\log\left(r_{\rm d}^{z}\right) = 0.09(\pm0.01) + 0.97(\pm0.01)\log\left(r_{\rm d}^{g}\right) \quad \Re^2 = 0.96, \quad (9)$$

$$\log\left(r_{\rm d}^{i}\right) = 0.04(\pm0.01) + 0.99(\pm0.01)\log\left(r_{\rm d}^{r}\right) \quad \Re^2 = 1.00, \quad (10)$$

$$\log\left(r_{\rm d}^{z}\right) = 0.03(\pm0.01) + 0.99(\pm0.01)\log\left(r_{\rm d}^{r}\right) \quad \Re^2 = 0.98, \quad (11)$$

$$\log\left(r_{\rm d}^{z}\right) = 0.00(\pm0.01) + 1.00(\pm0.01)\log\left(r_{\rm d}^{i}\right) \quad \Re^2 = 0.98. \quad (12)$$

Although scalelengths derived from different SDSS bands do not show significant differences, their general trends are as predicted by Cunow (1998). Typically, the correlations are very strong, and in almost all bands, the corresponding average scalelengths are comparable: $\langle r^{u}{}_{\rm d}\rangle = 5.12$ (±3.36) kpc, $\langle r^{g}{}_{\rm d}\rangle = 3.85$ (±2.10) kpc, $\langle r^{r}{}_{\rm d}\rangle = 3.79$ (±2.05) kpc, $\langle r^{i}{}_{\rm d}\rangle = 3.81$ (±2.05) kpc, $\langle r^{z}{}_{\rm d}\rangle = 3.75$ (±2.02) kpc.

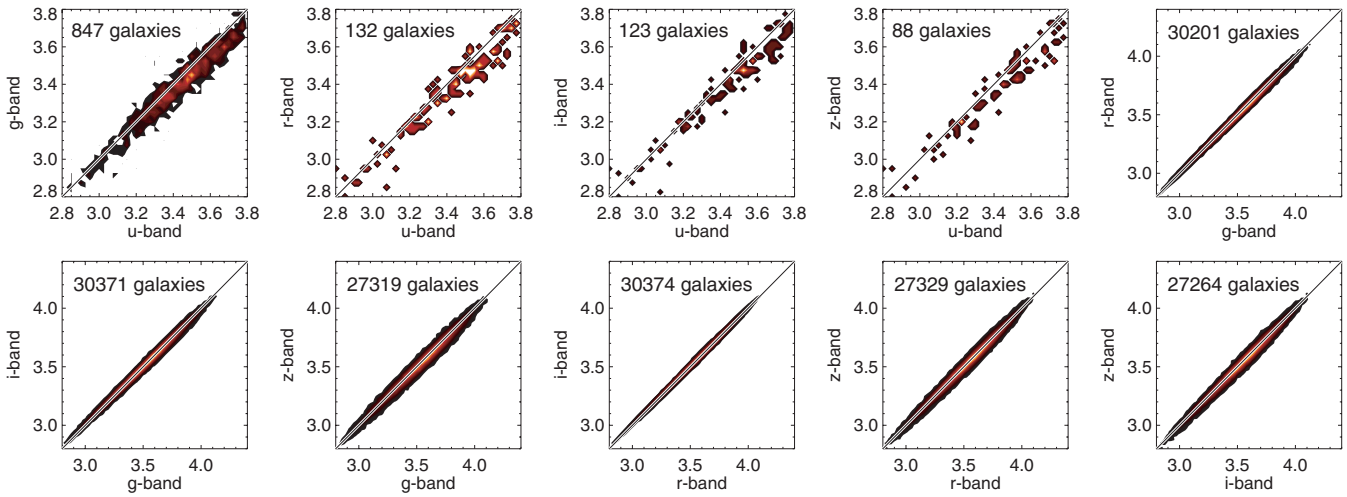

Figure 14. Scalelengths in *u*, *g*, *r*, *i*, *z* bands given in decimal logarithm of parsecs, with the number of points in each density plot stated, and the 1:1 line drawn on each panel.

We further find that these numbers are consistent with e.g. Courteau (1996), de Jong (1996) and de Grijs (1998) who presented an extensive analysis of deep images of 349, 86 and 45 spiral galaxies, respectively. It should be noted that the sample of de Grijs (1998) is a sample of edge-on galaxies, which explains the relatively insignificant variations found in our analysis, as opposed to theirs. Furthermore, their wavelength range, from B to K, is larger than with SDSS data. In an attempt to extend these results to compare with near-infrared results, we also cross-correlated our sample with the Two Micron All Sky Survey (2MASS) *J*-, *H*-, *K*-band images. We applied the code presented in Section 3 and found the 2MASS images are too shallow to yield anything presentable.

4.3 Scalelength versus stellar mass

We retrieve stellar masses for our sample galaxies by cross-matching our sample with the publically available sample of Kauffmann et al. (2003) and Brinchmann et al. (2004), and find stellar masses for 30 126 (i.e. almost all our sample) galaxies. These authors have calculated total stellar masses for nearly a million SDSS galaxies based on photometry of the outer regions of the galaxies with models that produce dust-corrected star formation rates and use upgraded stellar population synthesis spectra for the continuum subtraction. As noted by these authors, comparison between the stellar masses derived from photometry and spectra from the central regions shows that the fits to the photometry are more constrained at low mass since the emission-line contribution makes the line index fits less well constrained. Since the spectroscopic masses are based on fibre spectra from SDSS, which cover only a fraction of the galaxies, we opt to use the stellar masses from photometry.

In Fig. 15 we illustrate the scalelength as a function of total stellar mass, and find that larger mass galaxies have larger scalelengths. Moreover, we find that this increase is accompanied by a larger spread in scalelength. Galaxies with total stellar mass less than $10^8\,M_\odot$ have average *r*-band scalelength of 238 ± 94 pc, galaxies with total stellar mass between 10^9 and $10^{10}\,M_\odot$ have average scalelength of 1.52 ± 0.65 kpc, and galaxies with total stellar mass between 10^{11} and $10^{12}\,M_\odot$ have average scalelength of 5.73 ± 1.94 kpc. All points in Fig. 15 are also colour coded to show the consistently increasing intrinsic absolute magnitude for larger stellar mass galaxies.

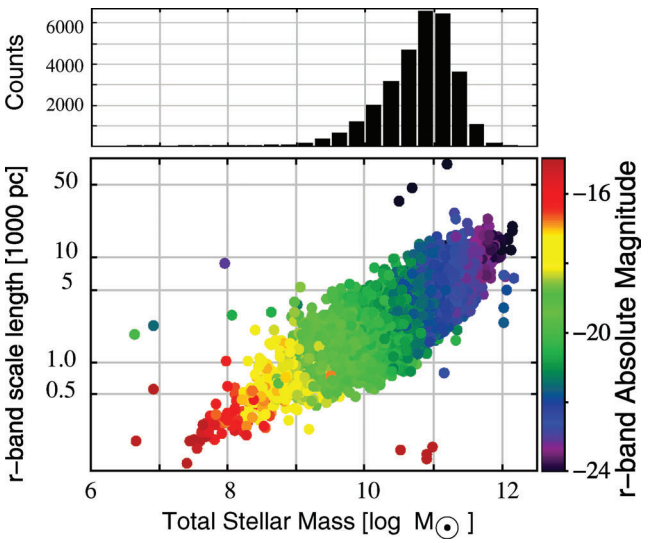

Figure 15. Total stellar mass distribution of our sample is illustrated in the top panel, and the scalelength versus mass diagram shows the expected behaviour in the bottom panel. The colour code shows the *r*-band absolute magnitude derived from the SDSS apparent *r*-band magnitude. The histogram and the scatter plot illustrate the same mass range.

5 DISCUSSION

We have derived reliable scalelengths for 30 374 disc/spiral galaxies, with no sign of ongoing interaction or disturbed morphology, in all five *u*, *g*, *r*, *i* and *z* bands from SDSS DR6 images. Cross-correlation of the SDSS sample with the LEDA catalogue has enabled us to investigate the variation of the scalelengths for different types of disc/spiral galaxies. Although the typical scalelength in *u* band is 35 per cent larger than that in the *r* band, the scalelengths in the *g*, *r*, *i* and *z* bands are similar and only become smaller on the average for late morphological types. This result remains consistent when using by-eye morphological classification or when using asymmetry parameter, concentration parameter or velocity dispersion as an indicator for galaxy morphological type. Our sample spans a range of total stellar masses between $10^{6.6}$ and $10^{12.2}\,M_\odot$ with a typical galaxy mass of $10^{10.8\pm0.54}\,M_\odot$, and shows that the while scalelength increases for more massive galaxies, the scalelength spread also increases with galaxy mass. Overall, these results are in full agreement with the recent work by Courteau et al. (2007).

Scalelength variations between bands are commonly studied to better understand the content and distribution of different stellar populations, metals and/or dust. A colour gradient is expected to increase from early-type spirals to late-type spirals, mainly due to extinction, which increases to later types. However, for Scd galaxies or later the colour gradient becomes smaller, because of decreasing amount of extinction (see e.g. Peletier & Balcells 1996; de Grijs 1998).

Changes in galaxy scalelength in different wavelengths can be attributed to extinction by moderate amounts of dust, with radial metallicity and age gradients as other contributing factors (Elmegreen & Elmegreen 1984; Peletier et al. 1994; Beckman et al. 1996). All these parameters will probably change as a function of redshift, enabling us to measure the variation of intrinsic scalelength with cosmological epoch. It is expected that the opacity of disc galaxies is expected to have been systematically higher in the past (e.g. Dwek 1998; Pei, Fall & Hauser 1999). The fact that the observed radial colour vary little suggests strongly that stellar population effects are not important here. Dust effects are studied by using radiative transfer models which take into account scattering as well as absorption by dust, and observationally by investigating the scalelength ratio in different bands as a function of inclination, i.e. optical depth. However, there are some degeneracies. Any tendency of the stars in the outer parts of discs to be bluer would tend to result in underestimated dust content. Any tendency of the dust to concentrate towards the centre would result in an overestimate of the bluer scalelengths, and would not be distinguishable photometrically from a tendency of the stars in the outer disc to be bluer (cf. Pohlen & Trujillo 2006; Azzolini, Trujillo & Beckman 2008; Erwin, Pohlen & Beckman 2008). Peletier et al. (1994, 1995) found that scalelength ratios could change, due to stellar population changes, by a factor of approximately 1.1–1.2 from blue to near-infrared (*K* band). This would correspond to a factor of about 1.03–1.06 from *g* to *z*. Since these numbers are very small, a very accurate analysis is needed to derive conclusions from the SDSS data base. Our results seem to first order in agreement with these numbers.

The derived scalelengths and our presentation of the transformation coefficients for converting observed scalelengths from one SDSS band to another, furthermore, are meant to be useful tools to test the results of cosmological galaxy formation models, whether numerical or semi-analytical.

In the future, we plan to add the stored parameters form the Galaxy Zoo[7] project to obtain a larger sample with morphological classifications (at this stage, detailed morphologies are not available), but also compare scalelength as a function environment, nuclear activity and colour gradients (e.g. comparing the sample with that of Hatziminaoglou et al. 2005). Many more parameters can be further investigated, and with the data and the derived parameters at hand, we now have the capability to continue this project in various and potentially unforeseeable directions.

ACKNOWLEDGMENTS

This work made use of EURO-VO software, tools and services. The EURO-VO has been funded by the European Commission through contract numbers RI031675 (DCA) and 011892 (VO-TECH) under the 6th Framework Programme and contract number 212104 (AIDA), under the 7th Framework Programme. We also acknowledge the use of NASA's SkyView facility (http://skyview.gsfc.nasa.gov) located at NASA Goddard Space Flight Center, the usage of the HyperLeda data base (http://leda.univ-lyon1.fr) and the TOPCAT software (http://www.starlink.ac.uk/topcat/). KF acknowledges support from the Swedish Research Council (Vetenskapsrådet), and the hospitality of ESO-Garching where parts of this work were done. KF also acknowledges support from Sergio Gelato for computer support, and fruitful discussions with Robert Cumming and Genoveva Micheva. Finally, we thank the referee Frederic Bournaud for insightful and encouraging comments which helped improve our manuscript.

Funding for the SDSS and SDSS-II has been provided by the Alfred P. Sloan Foundation, the Participating Institutions, the National Science Foundation, the US Department of Energy, the National Aeronautics and Space Administration, the Japanese Monbukagakusho, the Max Planck Society and the Higher Education Funding Council for England. The SDSS website is http://www.sdss.org/

The SDSS is managed by the Astrophysical Research Consortium for the Participating Institutions. The Participating Institutions are the American Museum of Natural History, Astrophysical Institute Potsdam, University of Basel, University of Cambridge, Case Western Reserve University, University of Chicago, Drexel University, Fermilab, the Institute for Advanced Study, the Japan Participation Group, Johns Hopkins University, the Joint Institute for Nuclear Astrophysics, the Kavli Institute for Particle Astrophysics and Cosmology, the Korean Scientist Group, the Chinese Academy of Sciences (LAMOST), Los Alamos National Laboratory, the Max Planck Institute for Astronomy (MPIA), the Max Planck Institute for Astrophysics (MPA), New Mexico State University, Ohio State University, University of Pittsburgh, University of Portsmouth, Princeton University, the United States Naval Observatory and the University of Washington.

REFERENCES

Abraham R. G., van den Bergh S., Glazebrook K., Ellis R. S., Santiago B. X., Surma P., Griffiths R. E., 1996, ApJS, 107, 1
Adelman-McCarthy J. K. et al., 2008, ApJS, 175, 297
Azzolini R., Trujillo I., Beckman J. E., 2008, ApJ, 679, L69
Baggett W. E., Baggett S. M., Anderson K. S. J., 1998, AJ, 116, 1626
Beckman J. E., Peletier R. F., Knapen J. H., Corradi R. L. M., Gentet L. J., 1996, ApJ, 467, 175
Bertin E., Arnouts S., 1996, A&AS, 117, 393
Boroson T., 1981, ApJS, 46, 177
Bournaud F., Elmegreen B. G., Elmegreen D. M., 2007, ApJ, 670, 237
Brinchmann J., Charlot S., White S. D. M., Tremonti C., Kauffmann G., Heckman T., Brinkmann J., 2004, MNRAS, 351, 1151
Burda P., Feitzinger J. V., 1992, A&A, 261, 697
Byun Y. I., Freeman K. C., 1995, ApJ, 448, 563
Ceverino D., Dekel A., Bournaud F., 2010, MNRAS, 404, 2151
Combes F., Elmegreen B. G., 1993, A&A, 271, 391
Conselice C. J., 1997, PASP, 109, 1251
Conselice C. J., 2003, ApJS, 147, 1
Conselice C. J., Bershady M. A., Dickinson M., Papovich C., 2003, ApJ, 126, 1183
Coulais A., Schellens M., Gales J., Arabas S., Boquier M., Chanial P., Messmer P., 2009, in Proc. 19th Conference on Astronomical Data Analysis Software and Systems, Sapporo, Japan
Courteau S., 1996, ApJS, 103, 363
Courteau S., Dutton A., van den Bosch F. C., MacArthur L. A., Dekel A., McIntosh D. H., Dale D. A., 2007, ApJ, 671, 203
Cunow B., 1998, A&AS, 129, 593
Cunow B., 2001, MNRAS, 323, 130
Cunow B., 2004, MNRAS, 353, 477
Dalcanton J. J., Spergel D. N., Summers F. J., 1997, ApJ, 482, 659
de Grijs R., 1998, MNRAS, 299, 595
de Jong R. S., 1996, A&A, 313, 45
de Vaucouleurs G., 1948, Ann. Astrophys., 11, 247
de Vaucouleurs G., de Vaucouleurs A., Corwin H. G., Jr, Buta R. J., Paturel G., Fouque P., 1991, Third Reference Catalogue of Bright Galaxies, Vols 1–3. Springer-Verlag, Berlin
Doi M., Fukugita M., Okamura S., 1993, MNRAS, 264, 832
Dutton A., 2009, MNRAS, 396, 141
Dwek E., 1998, ApJ, 501, 643
Elmegreen D. M., Elmegreen B. G., 1984, ApJS, 54, 127
Elmegreen B. G., Elmegreen D. M., Chromey F. R., Hasselbacher D. A., Bissell B. A., 1996, AJ, 111, 2233
Elmegreen B. G., Elmegreen D. M., Vollbach D. R., Foster E. R., Ferguson T. E., 2005, ApJ, 634, 101
Erwin P., Pohlen M., Beckman J. E., 2008, AJ, 135, 20
Fathi K., 2004, PhD thesis, Groningen University
Fathi K., Peletier R. F., 2003, A&A, 407, 61
Freeman K. C., 1970, ApJ, 160, 811
Fukugita M. et al., 2007, AJ, 134, 579
Giovanelli R., Haynes M., 2002, ApJ, 571, L107
Governato F. et al., 2010, Nat, 463, 203
Graham A. W., 2001, MNRAS, 326, 543
Graham A. W., de Blok W. J. G., 2001, ApJ, 556, 177
Graham A. W., Worley C. C., 2008, MNRAS, 388, 1708
Hatziminaoglou E. et al., 2005, MNRAS, 364, 47
Holwerda B., 2005, PhD thesis, Groningen University
Kauffmann G. et al., 2003, MNRAS, 341, 33
Kent S. M., 1985, ApJS, 59, 115
Knapen J. H., 2004, in ASSL Vol. 319, Penetrating Bars Through Masks of Cosmic Dust, p. 189
Knapen J. H., van der Kruit P. C., 1991, A&A, 248, 57
Knezek P., 1993, PhD thesis, Univ. Massachusetts
Kormendy J., Kennicutt R. C., Jr, 2004, ARA&A, 42, 603
Lauberts A., 1982, The ESO/Uppsala Survey of the ESO(B) Atlas. Kluwer, Dordrecht
Lin D. N. C., Pringle J. E., 1987, MNRAS, 225, 607
Loveday J., 1996, MNRAS, 278, 1025
MacArthur L. A., Courteau S., Holtzman J. A., 2003, ApJ, 582, 689
Martig M., Bournaud F., 2010, ApJ, 714, L275
Mo H. J., Mao S., White S. D., 1998, MNRAS, 295, 319

[7]http://www.galaxyzoo.org

Mosteller F., Tukey J., 1977, Data Analysis and Regression. Addison-Wesley, Reading, MA
Nilson P., 1973, Uppsala General Catalogue of Galaxies. Uppsala Astron. Obs. Annaler, Band 6
Paturel G., Petit C., Prugniel P., Theureau G., Rousseau J., Brouty M., Dubois P., Cambrésy L., 2003, A&A, 412, 45
Pei Y. C., Fall S. M., Hauser M. G., 1999, ApJ, 522, 604
Peletier R. F., Balcells M., 1996, in Minniti D., Rix H.-W., eds, ESO/MPA Proc., Spiral Galaxies in the Near-IR. Springer-Verlag, Berlin, p. 48
Peletier R. F., Valentijn E. A., Moorwood A. F. M., Freudling W., 1994, A&AS, 108, 621
Peletier R. F., Valentijn E. A., Moorwood A. F. M., Freudling W., Knapen J. H., Beckman J. E., 1995, A&A, 300, L1
Pohlen M., Trujillo I., 2006, A&A, 454, 759
Prieto M., Aguerri J. A. L., Varela A. M., Muñoz-Tuñn C., 2001, A&A, 367, 405
Romanishin W., Strom K. M., Strom S. E., 1983, ApJS, 53, 105
Sandage A., 1961, The Hubble Atlas of Galaxies. Carnegie Institution of Washington, Washington
Schade D., Lilly S. J., Crampton D., Hammer F., Le Fevre O., Tresse L., 1995, ApJ, 451, L1
Schaye J. et al., 2010, MNRAS, 402, 1536
Schombert J. M., Bothun G. D., Schneider S. E., McGaugh S. S., 1992, AJ, 103, 1107
Sérsic J. L., 1968, Atlas de Galaxias Australes. Observatorio Astronomico, Cordoba
Shimasaku K. et al., 2001, AJ, 122, 1238
Silk J., 2001, MNRAS, 324, 313
Simien F., de Vaucouleurs G., 1983, in Athanassoula E., ed., Proc. IAU Symp. 100, Internal Kinematics and Dynamics of Galaxies. Reidel, Dordrecht, p. 375
Valentijn E. A., 1990, Nat, 346, 153
van der Kruit P. C., 1987, A&A, 173, 59
van Driel W., Valentijn E. A., Wesselius P. R., Kussendrager D., 1995, A&A, 298, 41
Vorontsov-Velyaminov B. A., Arkipova V. P., Kranogorskaja A. A., 1963–1974, Morphological Catalogue of Galaxies. Trudy Sternberg Stat. Astr. Inst., Moscow, 32, 33, 34
Yamauchi C. et al., 2005, ApJ, 130, 1545
York D. G. et al., 2000, AJ, 120, 1579

This paper has been typeset from a TEX/LATEX file prepared by the author.